

FIGURES

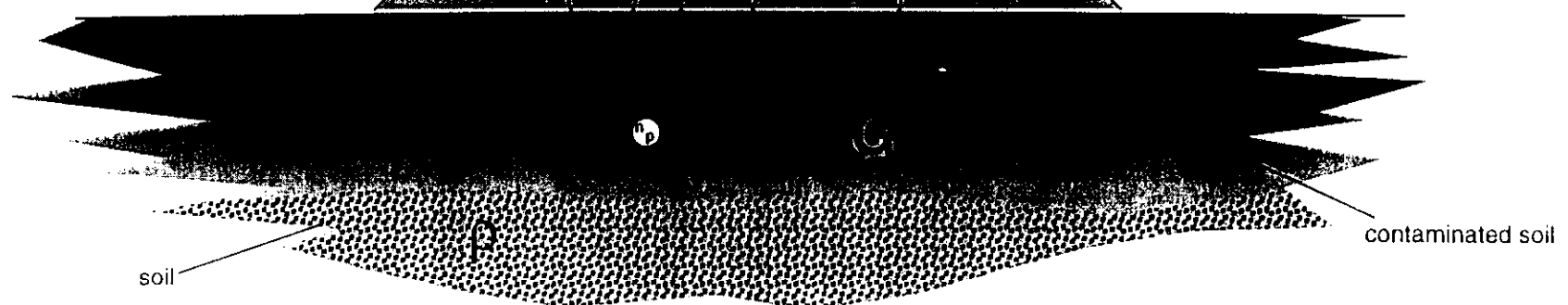
\mathcal{E} : some, but not all photon-detector interactions produce a valid "count" depending on the detector efficiency

γ : photon energy affects photon attenuation and thus the number of "counts" recorded per disintegration

detector

Σ

Ω : only photons traveling along a path contained within the sensor field of view will have a chance to interact with the detector



ρ : soil density affects photon attenuation and thus the number of "counts" recorded per disintegration

G: the source geometry (concentration and distribution) is the parameter solved for in the conversion process; normally distribution must be assumed in order to determine concentration

FIGURE 1

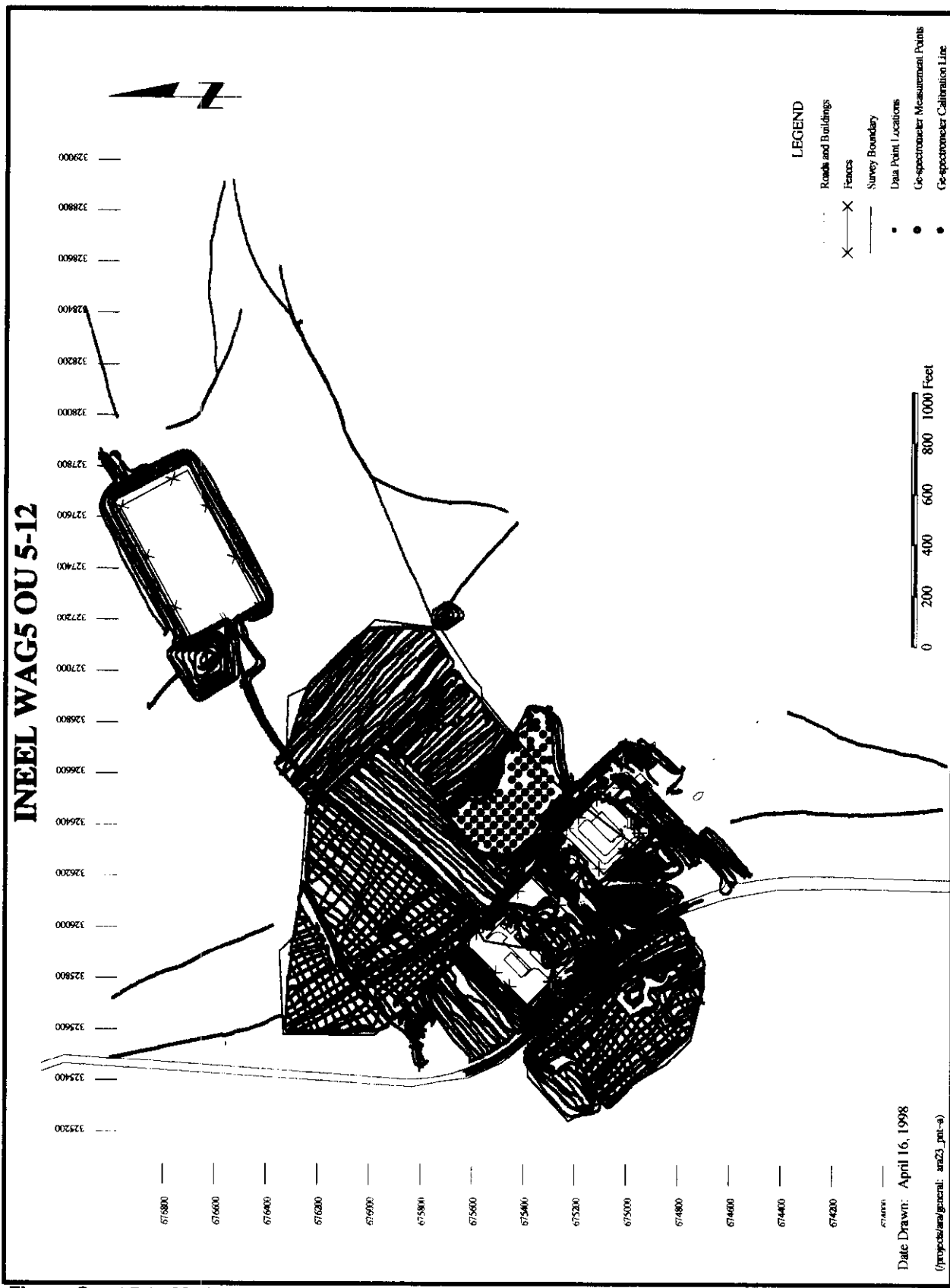


Figure 2. ARA-23, data point locations.

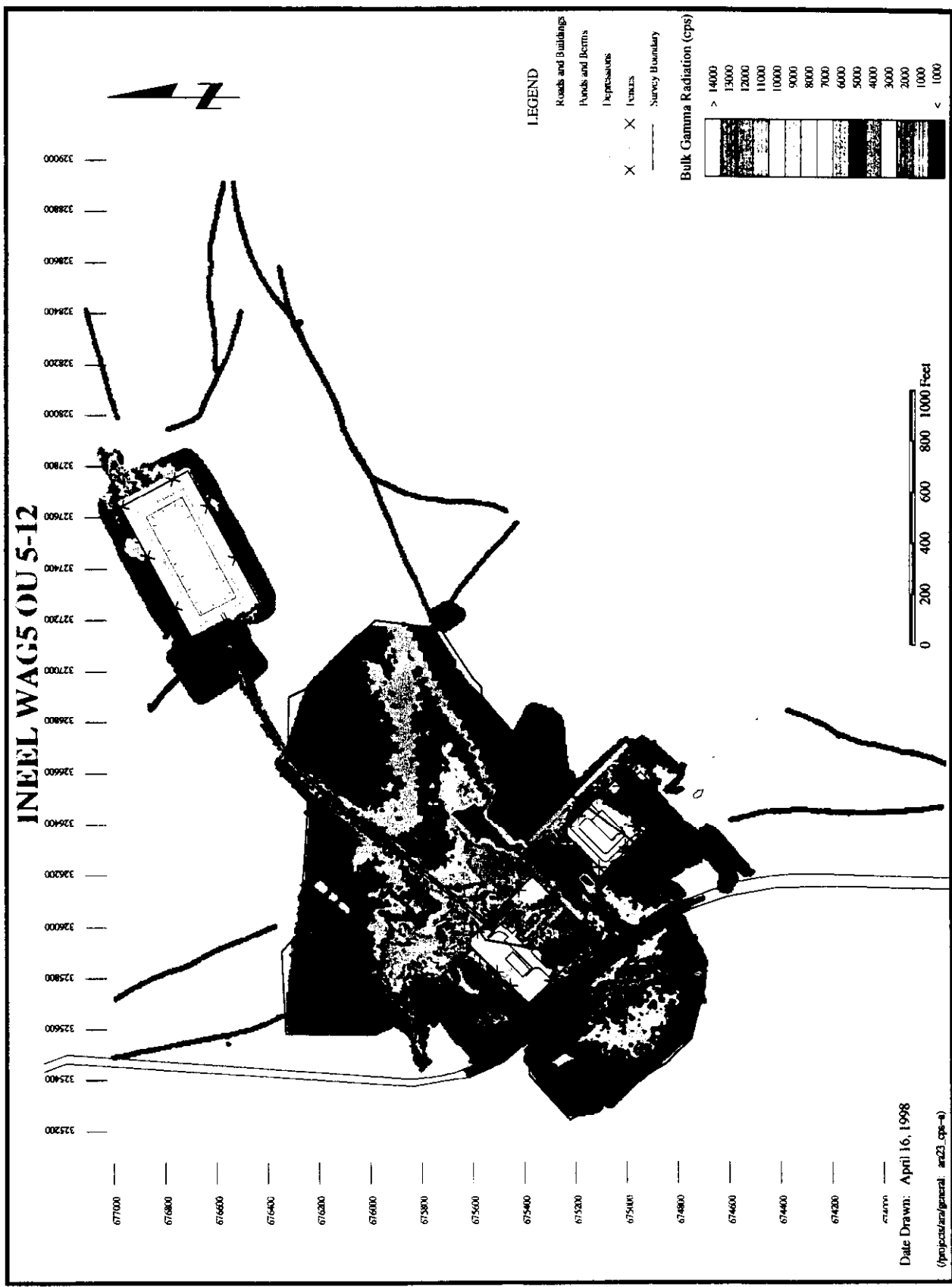


Figure 3. ARA-23, bulk gamma radiation.

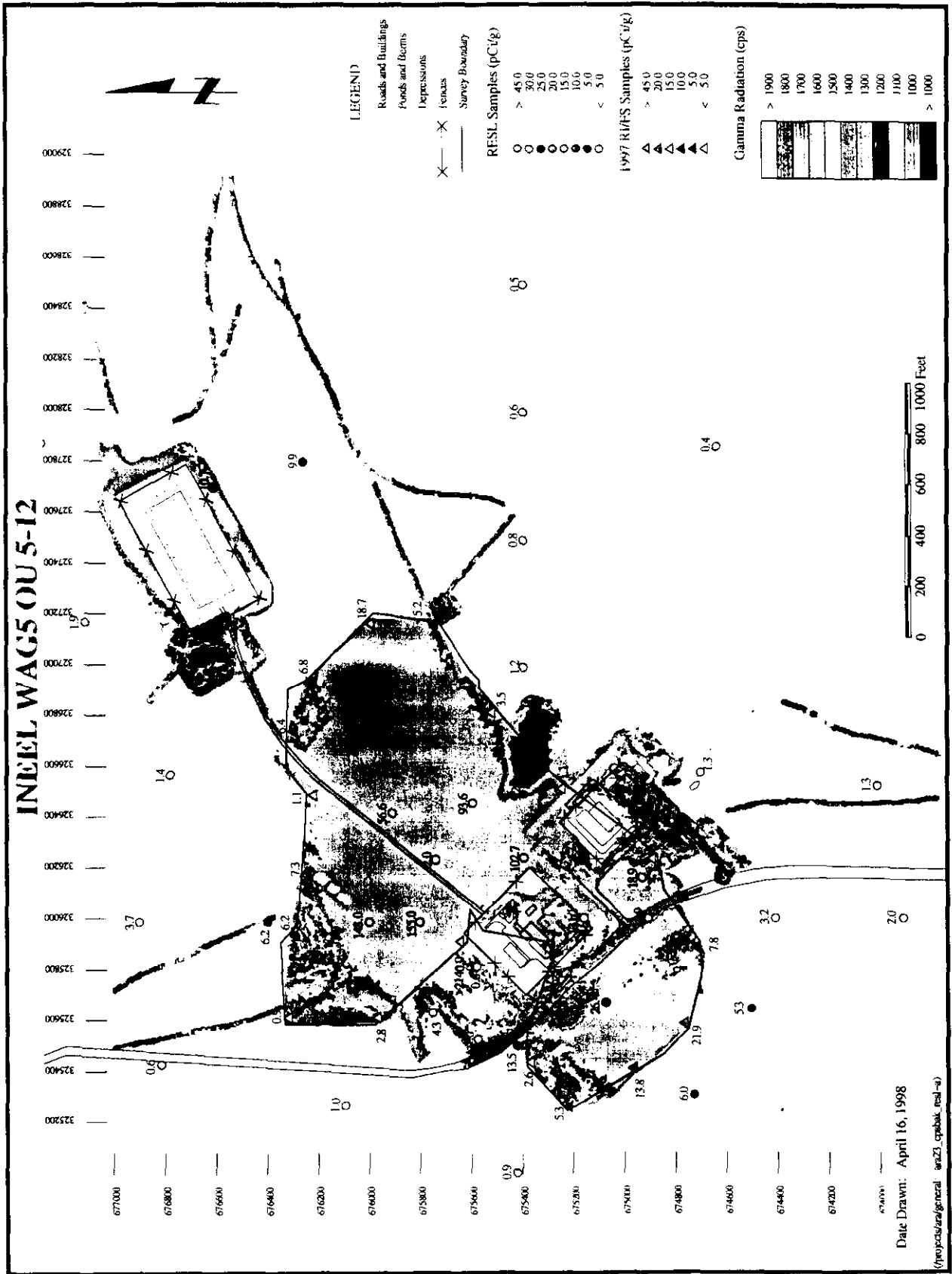


Figure 4. ARA-23, highlighted background radiation with sample locations.

Calibration Profile

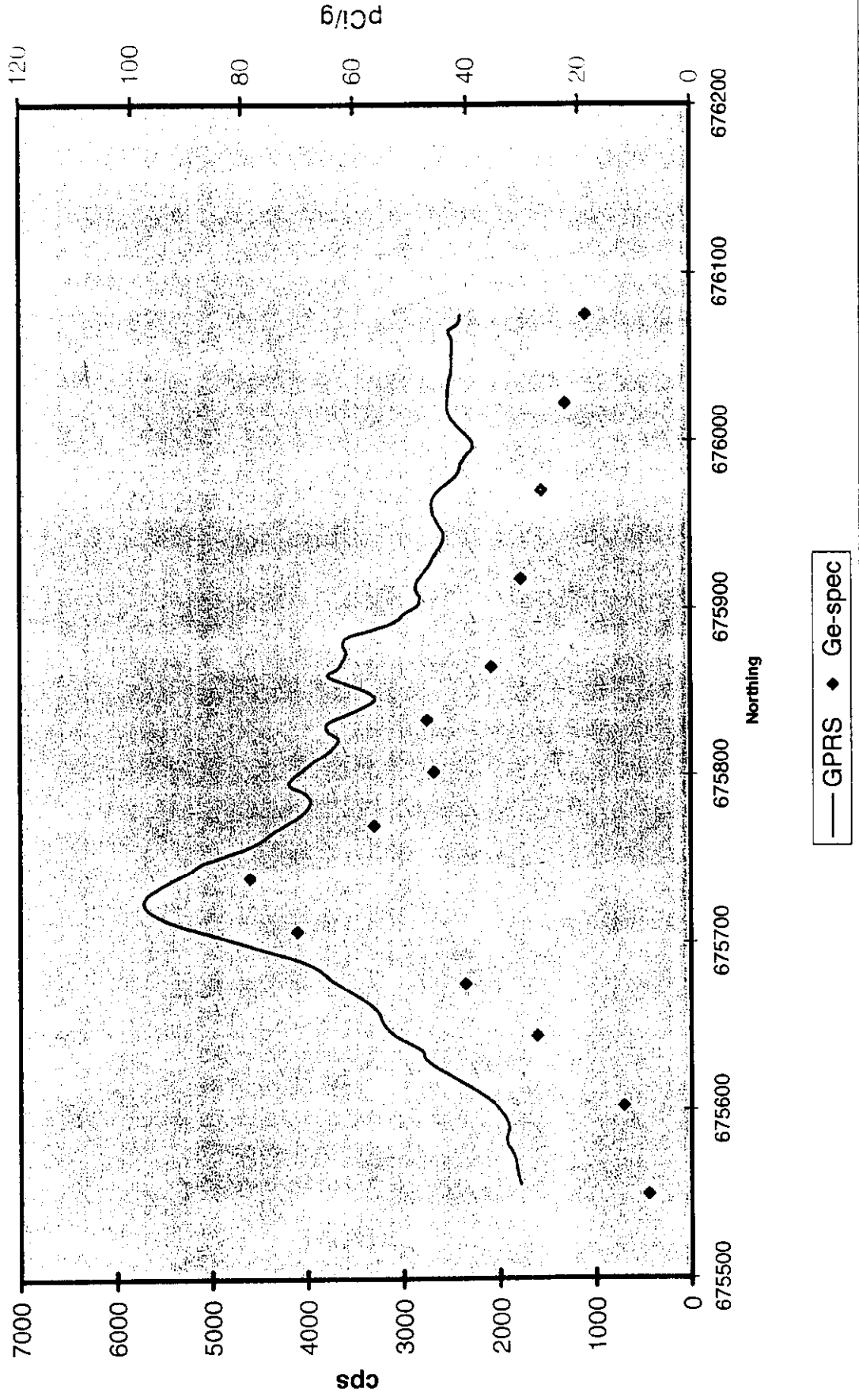


FIGURE 5

861-f

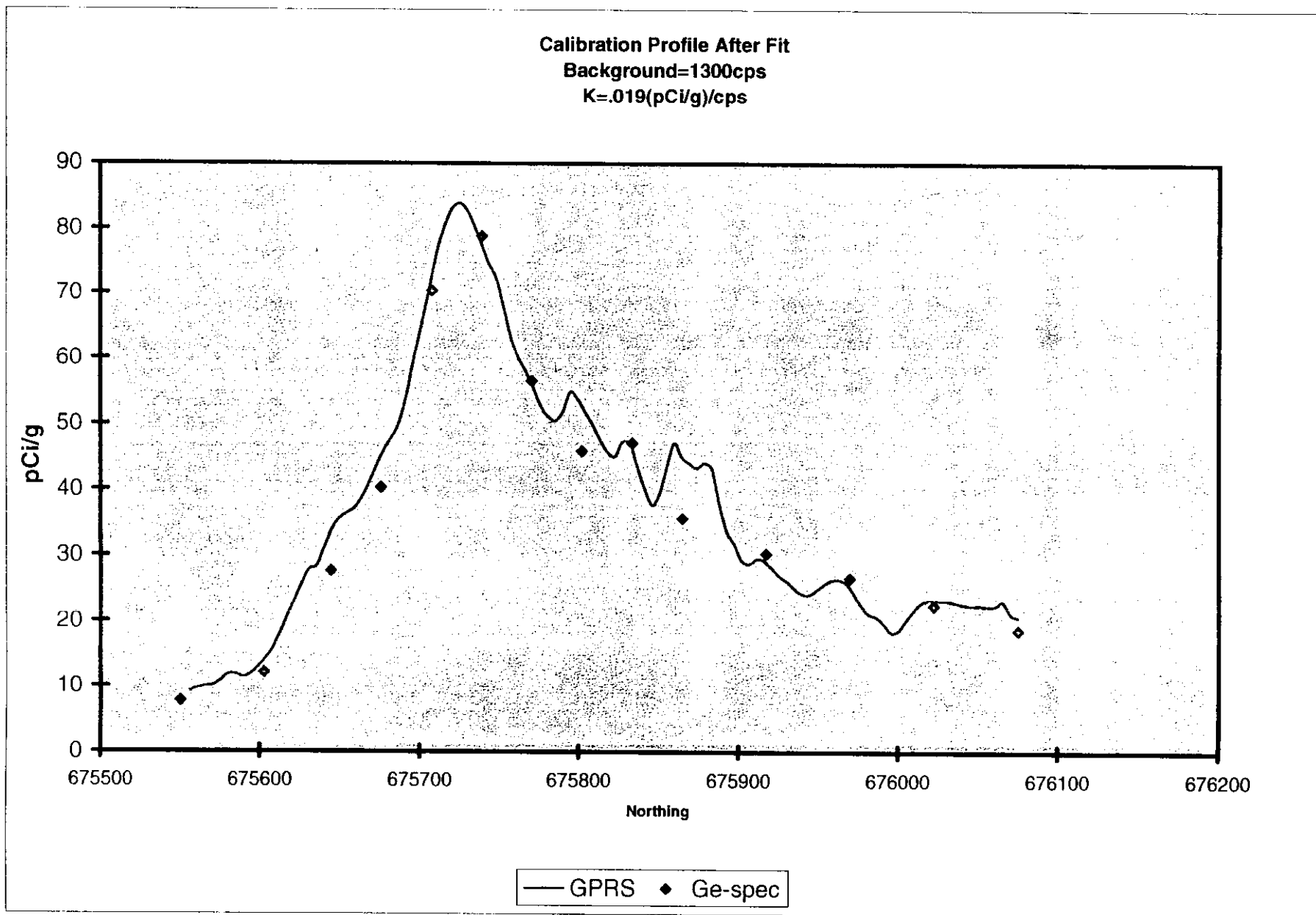


FIGURE 6

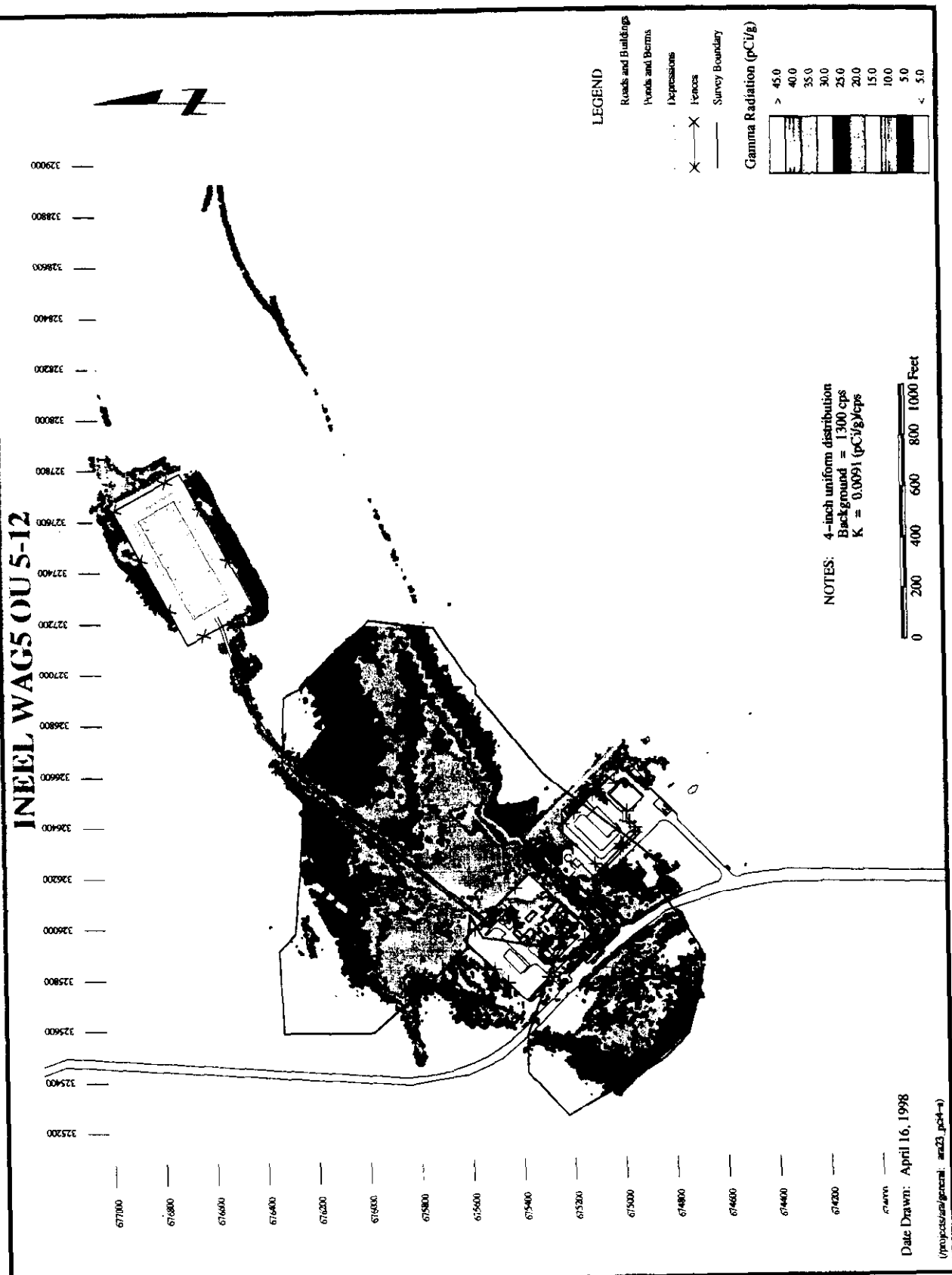


Figure 7. ARA-23, Cs-137 concentration.

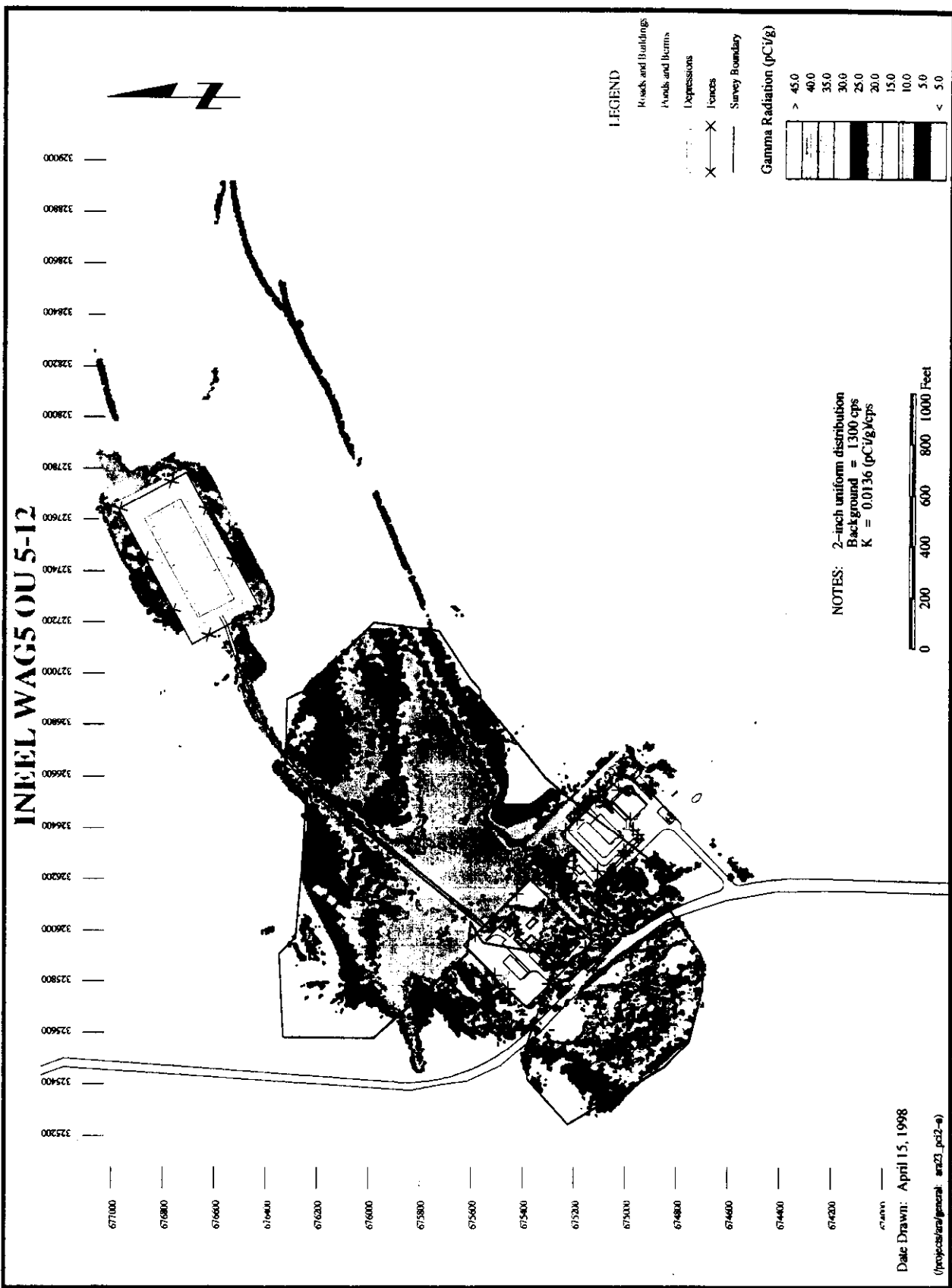


Figure 8. ARA-23, Cs-137 concentration.

INKEL WAGS OU 5-12

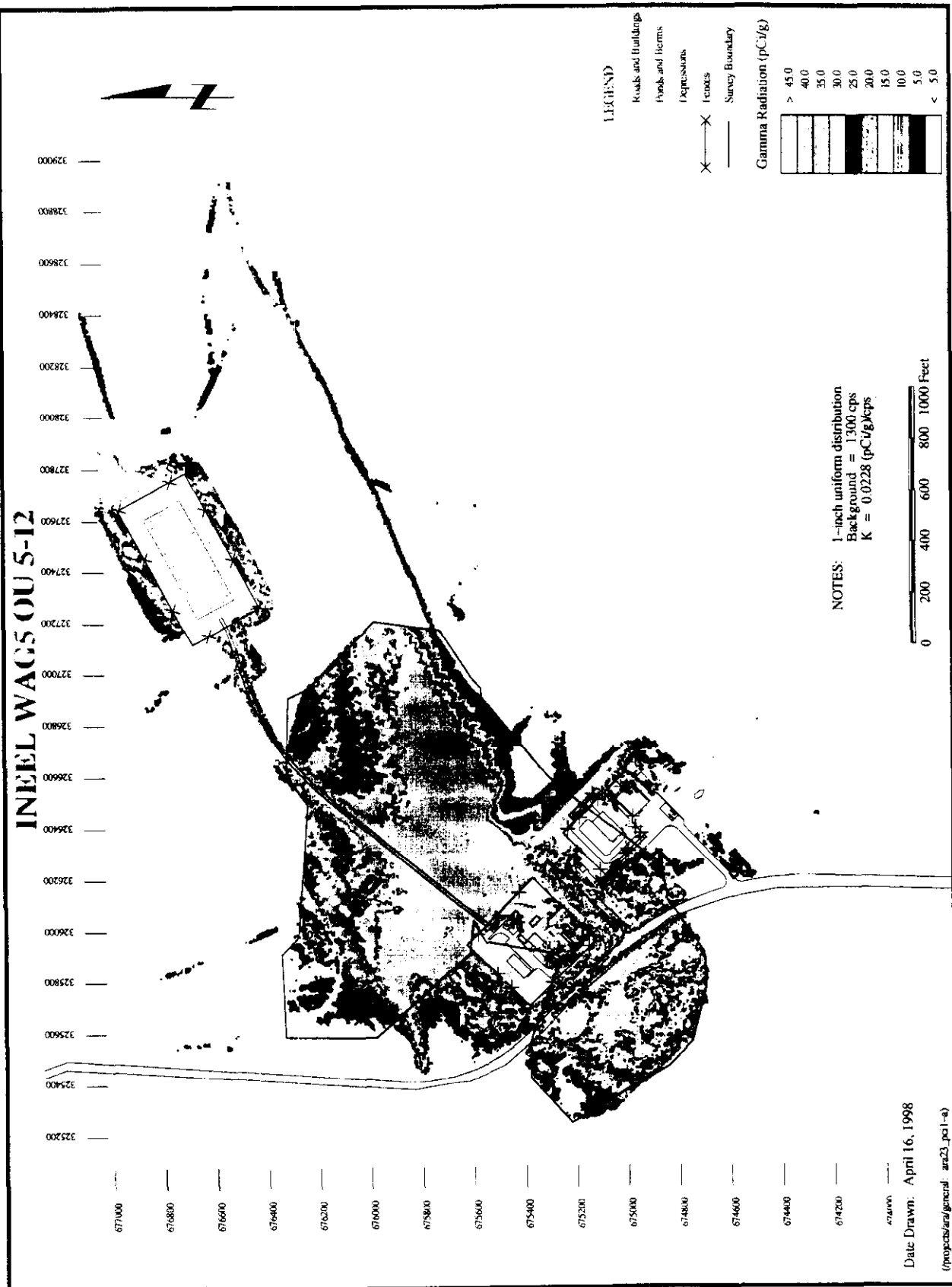


Figure 9. ARA-23, Cs-137 concentration.

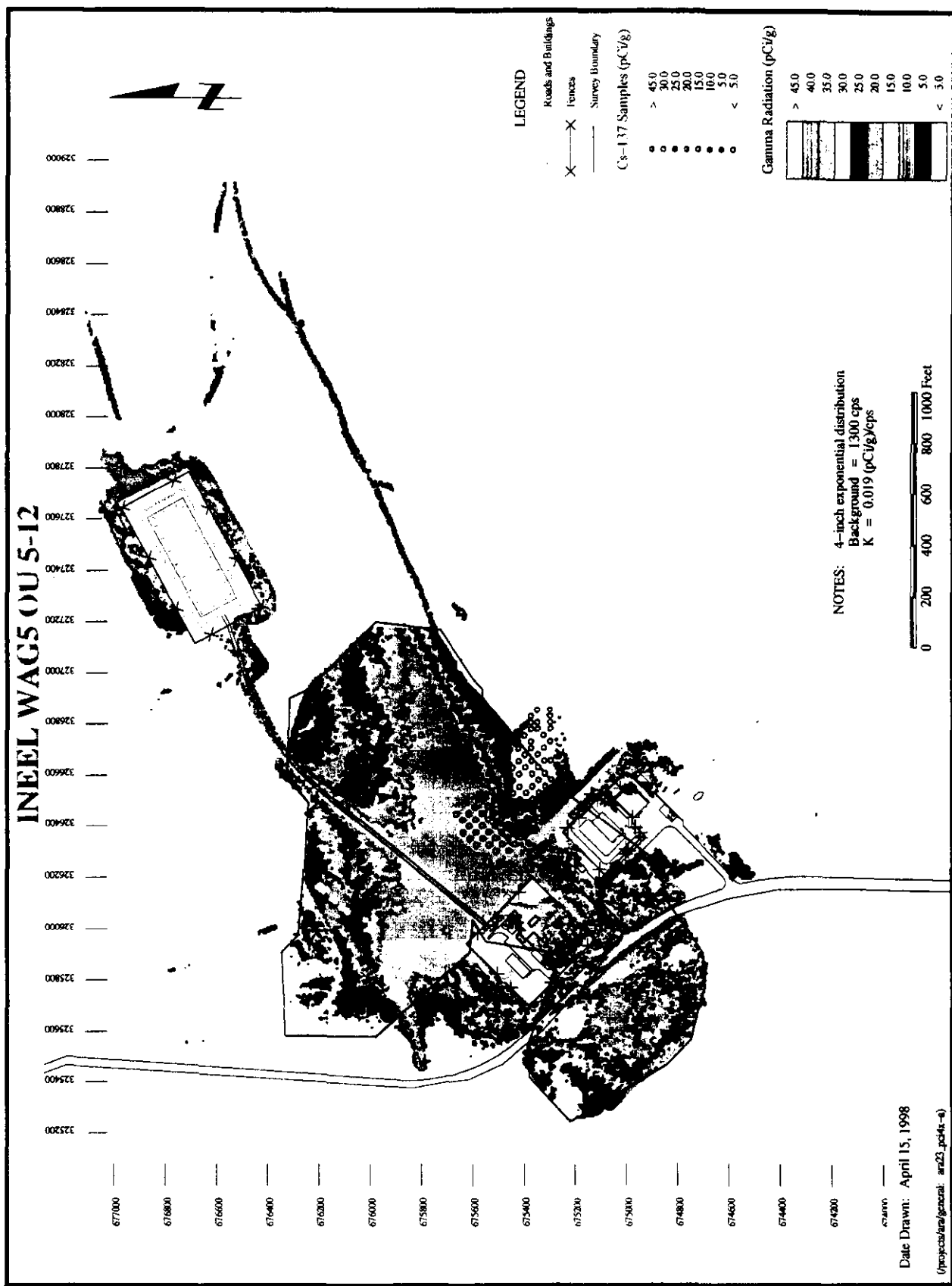


Figure 10. ARA-23, Cs-137 concentration and sample locations.

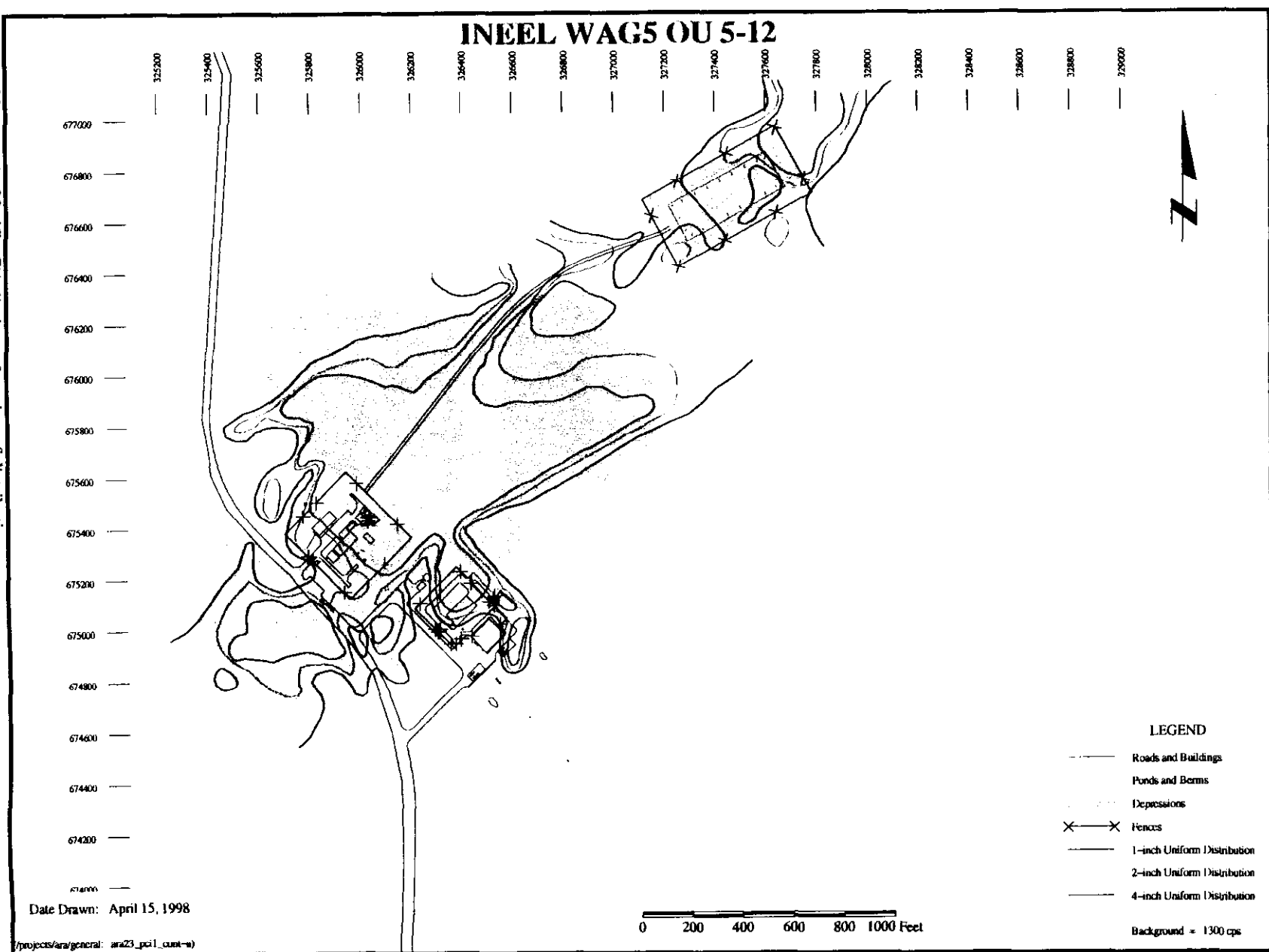


Figure 11. ARA-23, 17 pCi/g limits as function of distribution.

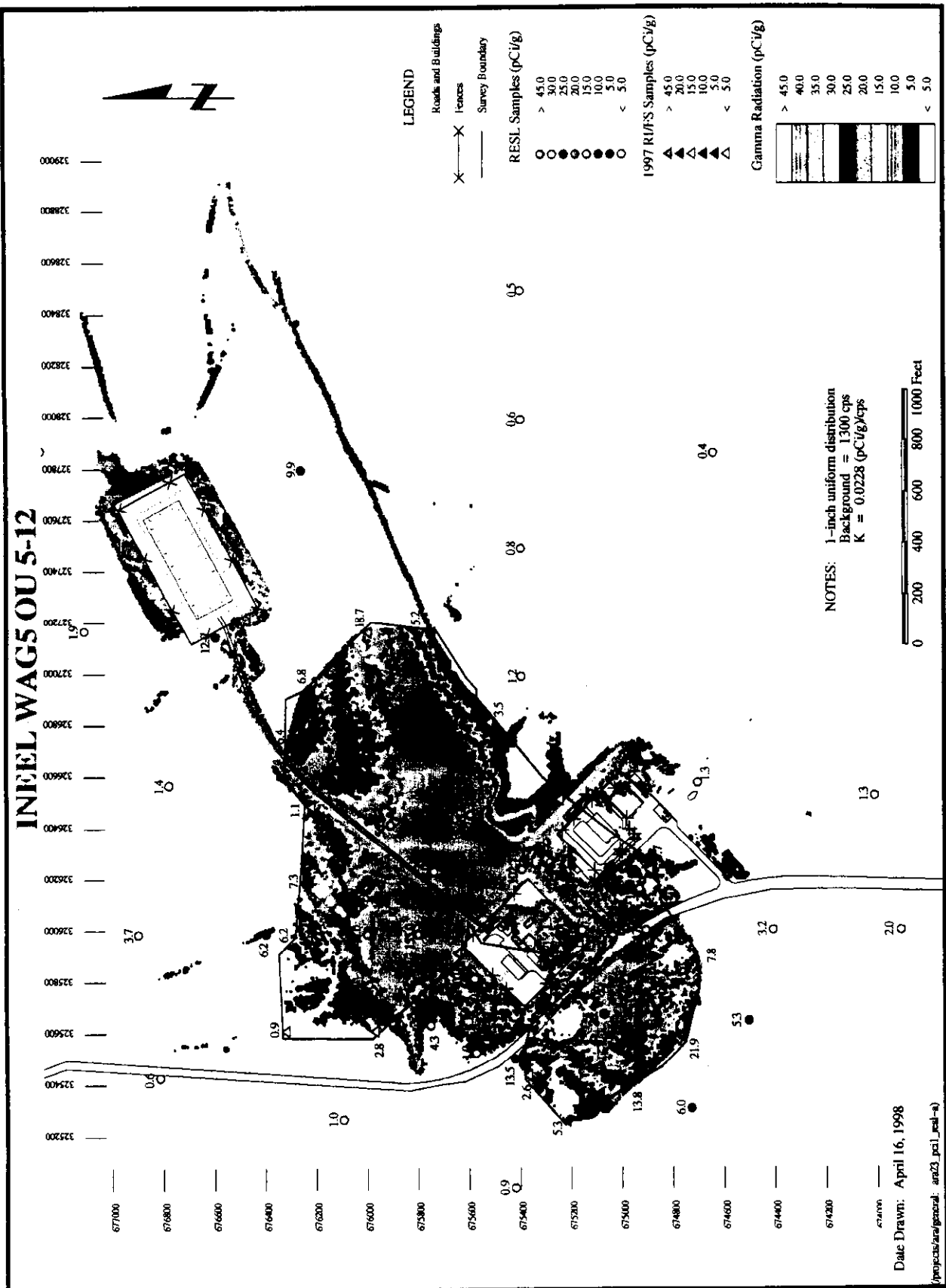
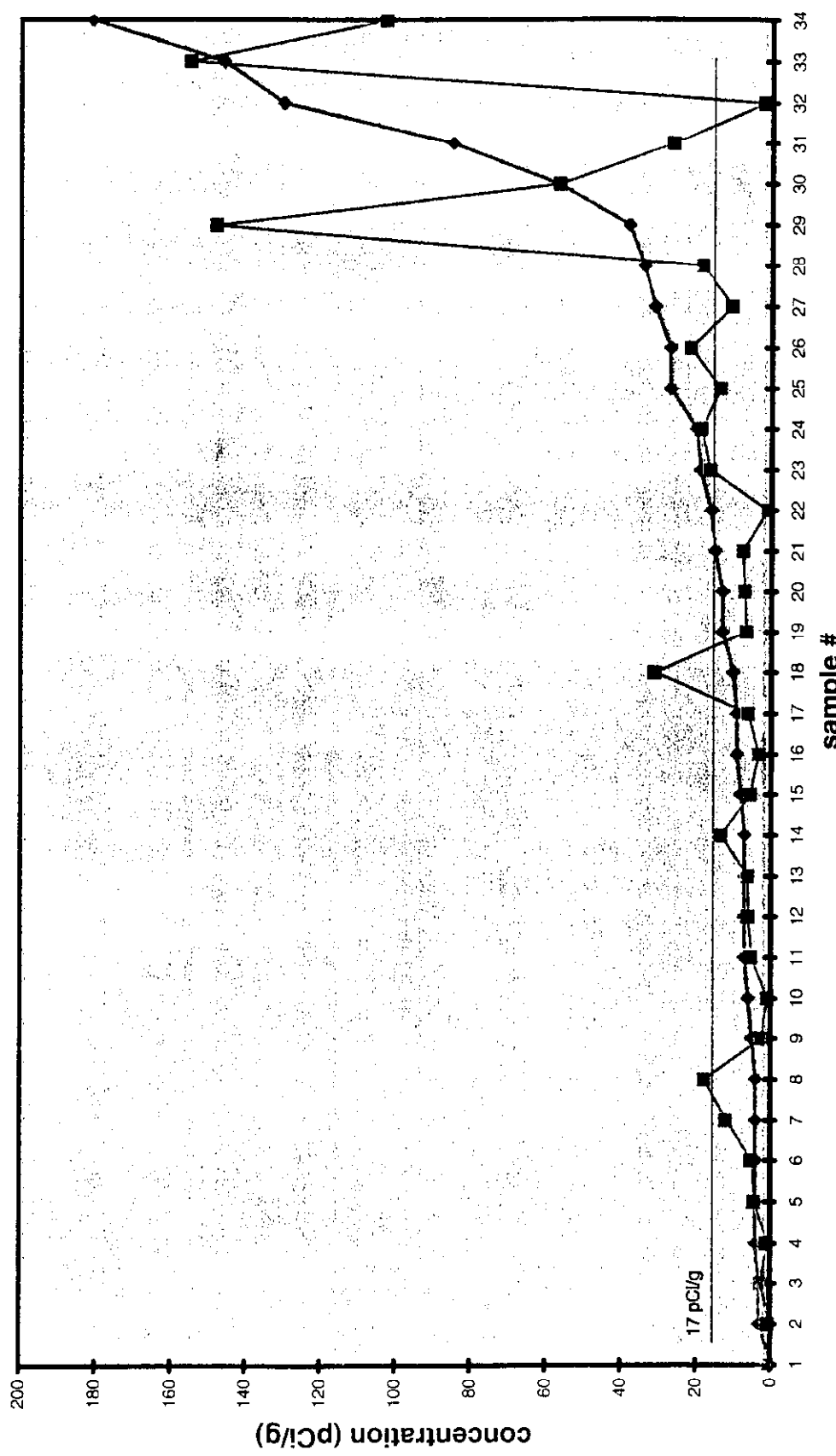


Figure 12. ARA-23, Cs-137 concentration with RESL and RI/FS sample locations.

Comparison between GPRS concentration estimates and sampling results



—♦— GPRS —■— Samples: RESL (black); perimeter (red)

FIGURE 13

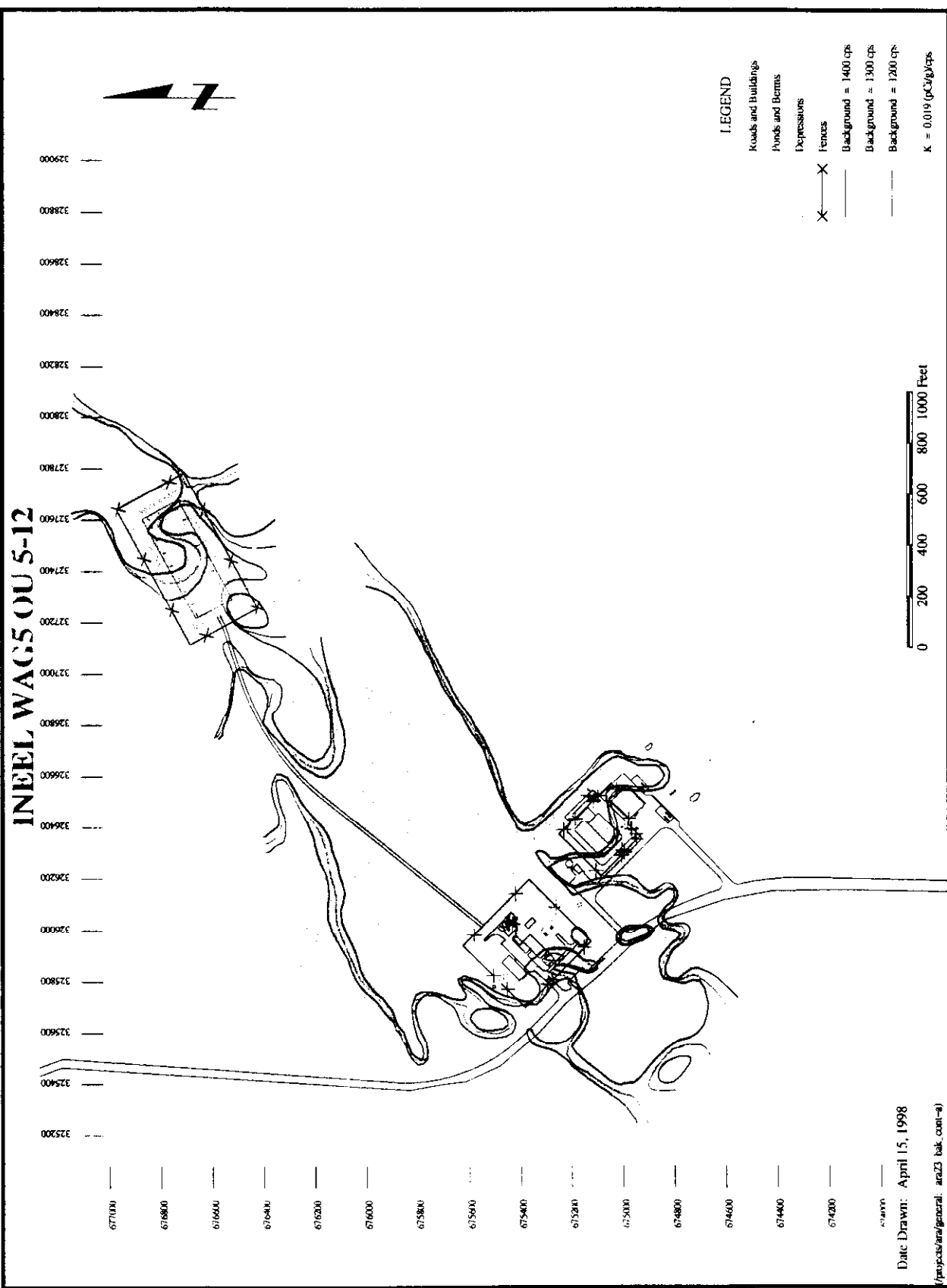


Figure 14. ARA-23, 17 pCi/g limits as function of background.



Figure 15. ARA-24, data point locations.

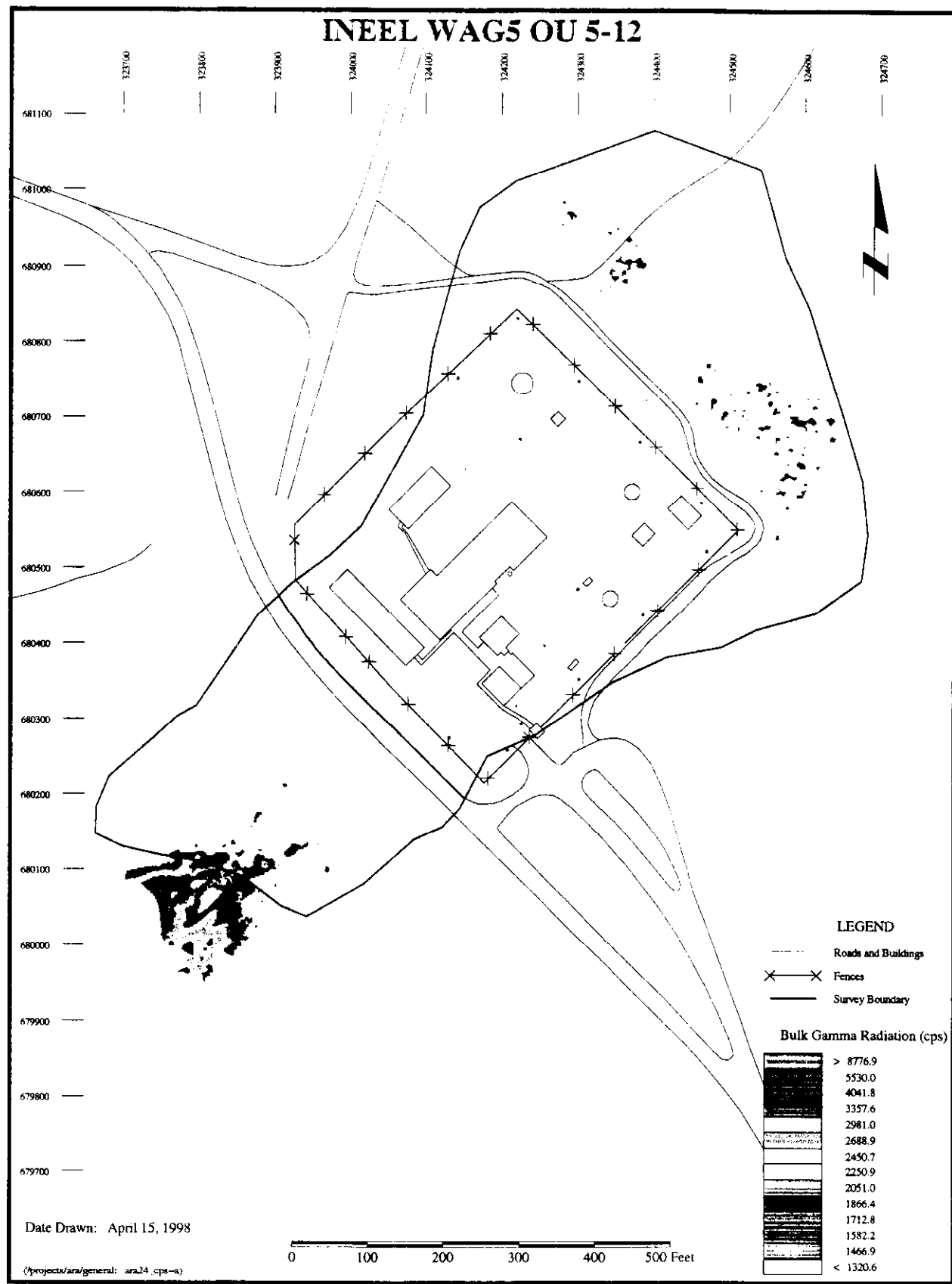


Figure 16. ARA-24, bulk gamma radiation.

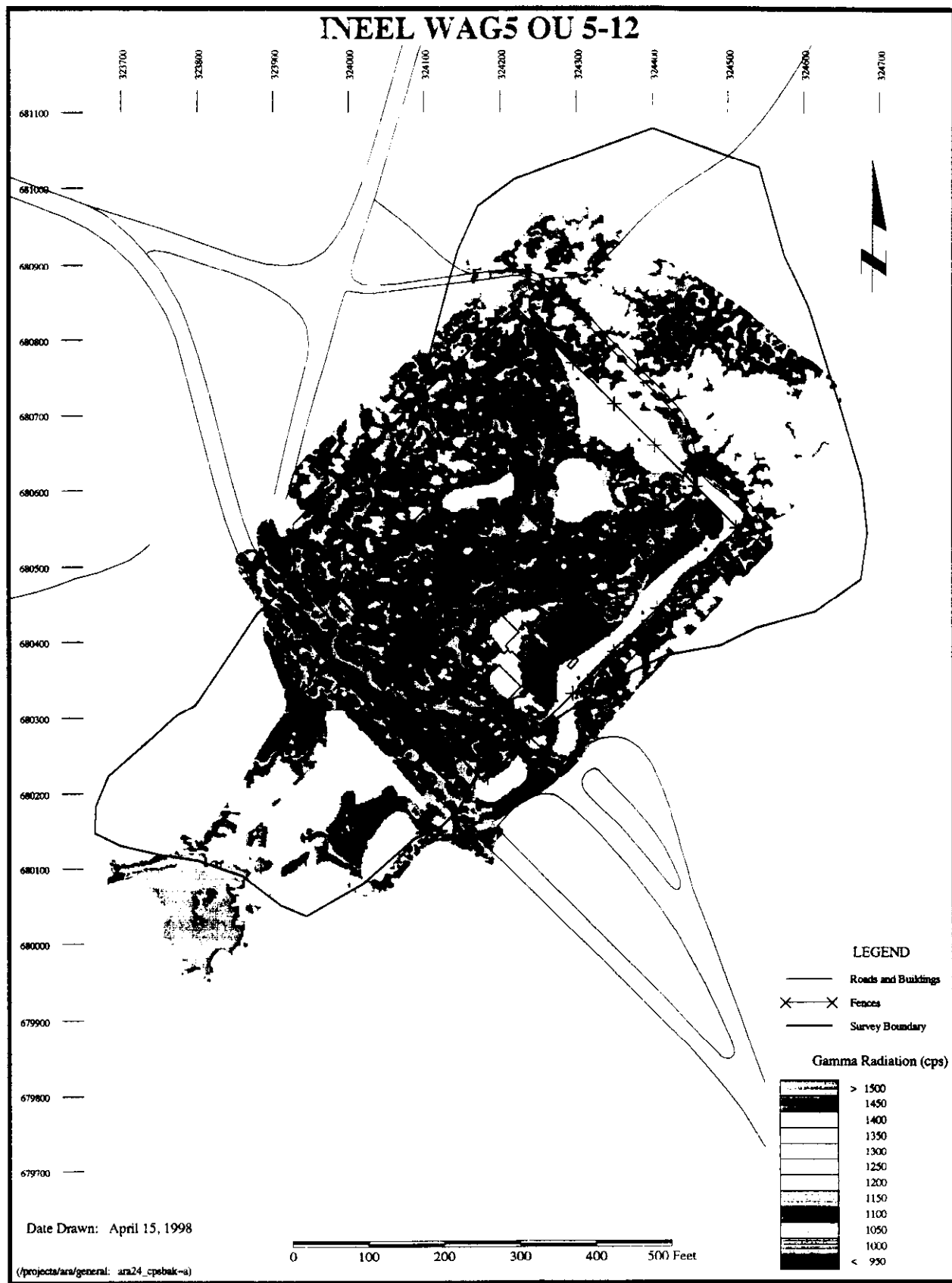


Figure 17. ARA-24, highlighted background radiation.

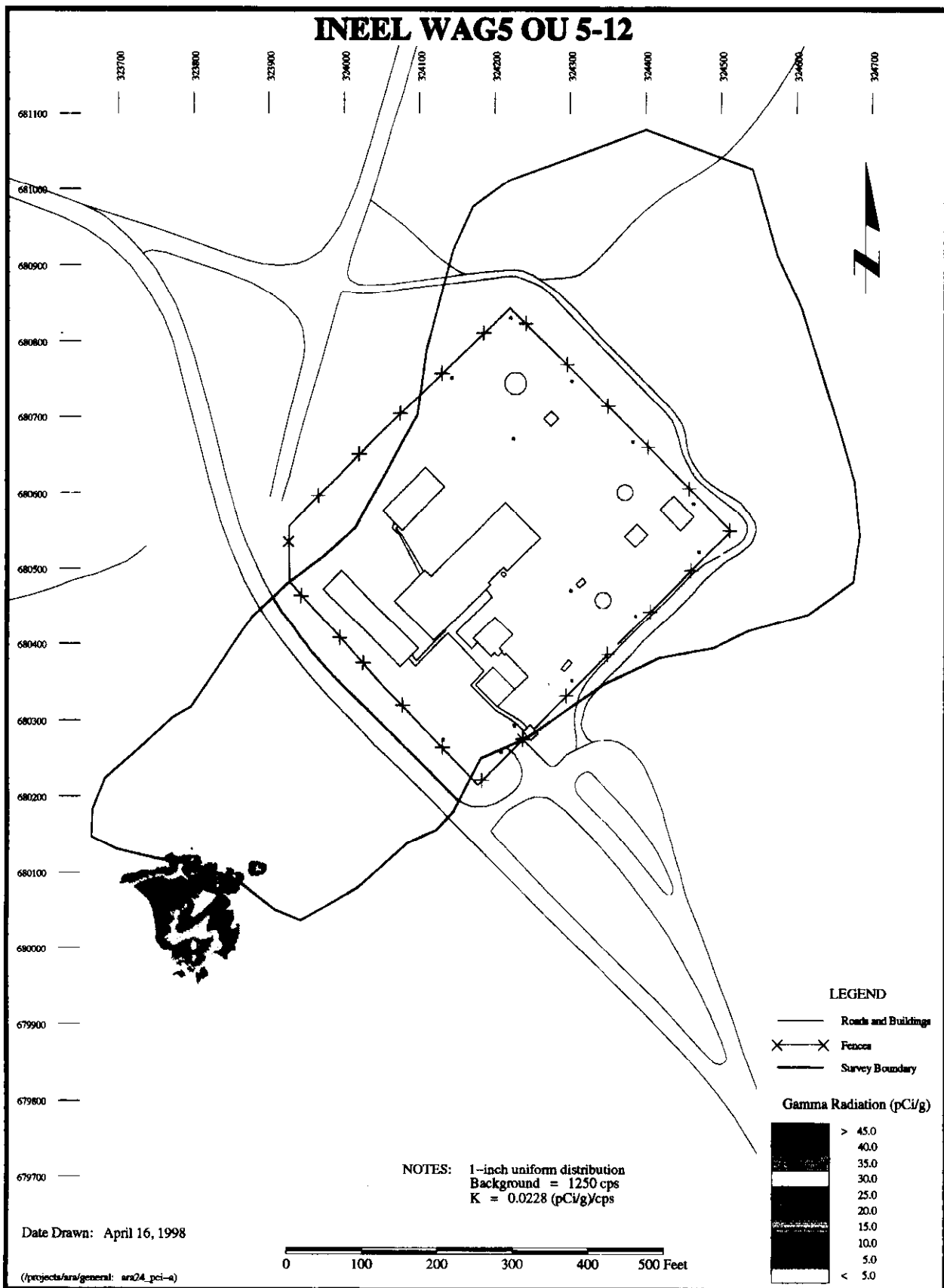


Figure 18. ARA-24, Cs-137 concentration.